Fluidized-bed measurements of carefully-characterized, mildly-cohesive (Group A) particles

CrossMark

C.Q. LaMarche, P. Liu, K.M. Kellogg, C.M Hrenya *

Department of Chemical and Biological Engineering, University of Colorado at Boulder, Boulder, CO 80309, USA

HIGHLIGHTS

- High-fidelity fluidized bed experiments are reported for mildly-cohesive glass beads.
- Characterized particle properties include friction, shape and restitution coefficient.
- Surface roughness is measured with AFM and is important to predicting cohesive forces.
- Defluidization experiments (pressure drop and bed density vs velocity) are reported.
- Bubble chord-length, velocity and frequency are presented for various axial and radial positions.

ABSTRACT

Fluidization is sensitive to mild cohesion levels, as evidenced by the different flow behaviors of Geldart Group A and Group B particles. Additionally, cohesion is extremely sensitive to surface roughness. Here, mildly cohesive (Group A) spherical particles were carefully characterized and used in high-fidelity experiments of defluidization, bed expansion, and bubble characterization. The experiments were conducted such that van der Waals forces were the only source of cohesion, and thus the results presented can be used for validating Discrete Element Method (DEM) and/or continuum models. Particle characterization includes surface roughness and adhesion (pull-off) force, which can be used for modeling the van der Waals force. Additionally, the particle friction coefficient, coefficient of restitution, shape (sphericity), and diameter were measured via a suite of simple experiments. This level of particle characterization, which is critical for the validation of cohesive models (DEM and continuum), has not been reported in previous fluidization studies. Accordingly, the characterization experiments employed here are described in sufficient detail for straightforward adaption elsewhere.

© 2016 Elsevier B.V. All rights reserved.

1. Introduction

Unit operations involving solid particle flows (fluidized beds, hopper flow, pneumatic transport lines, etc.) are characterized by complex hydrodynamics such as bubbling, clustering, and species segregation. Modeling frameworks such as the two-fluid (continuum) approach and Discrete Element Method (DEM) can increase the understanding of macro-scale behavior, which is linked to micro-scale (particle) properties [1]. For instance, DEM simulations have shown [2] particle-particle cohesion to be critical to homogenous bed expansion of mildly cohesive (Geldart Group A) particles. Also, past studies have found other particle properties, e.g., friction

coefficient [3], coefficient of restitution [4], and roughness [5], significantly affect the behavior of many-particle systems. A significant amount of recent DEM and experimental work has been targeted at understanding the effects of such properties on, for instance, fluidization behavior [2,6–16]. Nonetheless, although a large body of experimental data exists using cohesive and non-cohesive particles (e.g. Refs [17–32]), many of these studies do not report or include direct measurements of the particle properties necessary for a robust validation of models [17]. Accordingly, a detailed, comprehensive data set of fluidization behavior with carefully characterized particles is necessary, especially for mildly cohesive particles, which are particularly sensitive to micro-scale properties like roughness [5,6].

Numerous past works have demonstrated the important impact of particle properties on the fluidization behavior of non-cohesive systems. For example, for different types of glass (soda lime,

* Corresponding author at: University of Colorado, 596 UCB, Boulder, CO 80309, USA.
E-mail address: Hrenya@colorado.edu (C.M Hrenya).

borosilicate, etc.), tabulated values of kinetic (sliding) friction coefficient span 0.1 to 0.3 [24,33], and the defluidization curve (pressure drop vs. gas velocity) is known to change within this range [33]. Furthermore, several groups have found that the coefficient of restitution significantly affects bubble properties [4,34,35], but it negligibly affects the defluidization curve [33]. It was also found that accounting for even a slight non-sphericity (sphericity > 0.92) is necessary to predict defluidization accurately with DEM [33]. Additionally, previous works have indicated that particle size [36] and the width of the particle size distribution [37] impact bubble properties. Collectively, these studies point to the importance of particle properties on fluidized bed behavior and the corresponding need for carefully characterized particles.

In addition to the particle properties mentioned above [16,32,36], mildly cohesive (Group A) particles are also affected by other particle and system properties that are generally negligible for non-cohesive particles. The mild cohesion associated with Group A particles is attributed to the van der Waals force between particles [38], which is extremely sensitive to surface roughness; namely, the van der Waals cohesion is proportional to the square of the separation distance [39]. This sensitivity has been observed both in micro-scale (single-particle) [40] and macro-scale (many-particle) experiments [7,10,41]. Furthermore, recent work [6] indicated that correctly accounting for surface roughness is critical to accurate defluidization predictions. Even though the dependence of cohesive particle behavior on surface roughness is well-documented, surface roughness measurements are rarely reported for many-particle experiments or reported in a form that is not sufficient for inputs into simulations. As an example of the latter, earlier studies provided scanning electron micrograph (SEM) images of their particles [7,42–44]. Such images provide high-resolution information about surface roughness in the lateral direction, but only qualitative information normal to the surface (since it is a two-dimensional projection of the surface) [45]; it is the normal direction that is critical to predicting van der Waals forces since it dictates the minimum separation distance between particles.

To account for the effects of surface roughness in cohesive models for DEM and continuum frameworks, roughness must be measured accurately. Atomic Force Microscopy (AFM) can be used to quantify surface via topographical maps with nanoscale resolution [46]. The links between surface roughness and adhesion forces have been investigated in several studies, e.g. [47–51]. Two approaches are available to incorporate such roughness measurements into models for van der Waals forces: (i) analytical solution of single-equation theories that incorporate roughness (e.g. the Hamaker theory adjusted to account for surface roughness [40,47,52–55]), and (ii) computational methods that sum the van der Waals force between adjacent points on discretized meshes that reproduce the measured the surface roughness [56–60]. Regarding the former, a method was recently developed to extract roughness parameters from the measured particle topography, without resorting to visual or arbitrary means, that can be used as input to the analytical theory [47].

The main aim of this work is to provide high-fidelity experimental data that can be used for validating DEM and/or continuum models that incorporate van der Waals forces. To achieve this aim, a twofold approach is implemented: (i) careful characterization of particles that are mildly cohesive (microscopic), and (ii) corresponding fluidized-bed measurements (macroscopic). Particles are characterized by measuring properties such as coefficient of friction, shape, coefficient of restitution, and surface roughness using straightforward techniques. Pressure drop and bed expansion are reported with increasing and decreasing gas velocity (fluidization and defluidization). Furthermore, bubble size, frequency and velocity are presented for particles with increasing cohesion at various gas velocities and axial and radial positions.

2. Materials and experimental methods

2.1. Particles

Soda-lime glass spheres from Mo-Sci Corp were used in this work. To ensure the particles are close to monodisperse, they were sieved to the smallest size range possible using standard sieves. Specifically, the three size ranges implemented here are 20–38 μm, 45–53 μm, and 63–75 μm. Fig. 1 shows that the particles are relatively monodisperse (narrow particle size distribution) and nearly spherical, making them close to ideal for validating DEM and continuum theories. Table 1 provides the particle properties specific to each size range, namely, the mean diameter (d_p) and particle shape (sphericity, ϕ); the technique used to measure the sphericity will be detailed in the following section.

2.1.1. Particle characterization: sphericity, restitution coefficient, and friction coefficients

Particle size and material density (ρ_p) are the most commonly reported material parameters in past works, likely because they are reported by manufacturers and/or straightforward to measure (e.g. sieve analysis for determining particle size). For this work, simple, and relatively inexpensive methods were developed to measure the other relevant particle properties (shape (sphericity) ϕ, restitution coefficient e, static friction coefficient μ_s, and kinetic friction coefficient μ_k) with the intent of making these techniques easily adoptable in most labs. As detailed below, the coefficients of friction and restitution were measured using a DVC (model 340 M) high-speed camera, and the acquisition rate used varied between 100 and 300 frames per second (fps) based on the requirement of the system (i.e. faster particle velocities required faster frame rates) and the amount of light available in a given experiment. The image resolution was generally 320 pixels x 240 pixels. This high-speed camera is the most expensive piece of equipment for this suite of measurements; however, many current point-and-shoot cameras offer comparable high-speed video acquisition with frame rates of around 250 fps. In order to eliminate cohesion in the restitution and friction measurements, tests were performed using 2 mm diameter soda-lime glass spheres from the same distributor as those used in the fluidized-bed experiments.

Fig. 2 provides images that overview these straightforward characterization techniques. As pictured in Fig. 2a–c, the coefficient of restitution is measured using a laboratory ring stand with several clamps used to hold a pair of tweezers. The tweezers clamp onto a particle (a 2 mm glass bead is held by the end of the tweezers in Fig. 2a), which uses a spring-based clamp to hold the particle, allowing the tweezers to open wider than the particle when unclamped. The particle motion is recorded with the high-speed camera to obtain the height when released, h_o (Fig. 2a) and the maximum height after rebound, h_f (Fig. 2c) using a ruler in the frame of the image. The restitution coefficient is then determined according to $e = \sqrt{h_f/h_o}$. To ensure an accurate measurement of e, only normal particle-wall collisions with no particle rotation can be considered. Accordingly, if the particle bounces at an oblique angle, the trial is rejected as it indicates significant spin was imparted on the particle during release; usually this behavior is associated with incorrectly releasing the tweezers.

Fig. 2d shows the method to measure particle shape, or sphericity, using images taken with an optical microscope, which is the particle projected area diameter divided by the projected perimeter diameter [33,61].

The particle-particle and particle-wall coefficient of friction measurements are described in detail elsewhere [62], with an image of the apparatus provided in Fig. 2e. To measure the kinetic (sliding) friction coefficient, a sled is made of particles glued to a
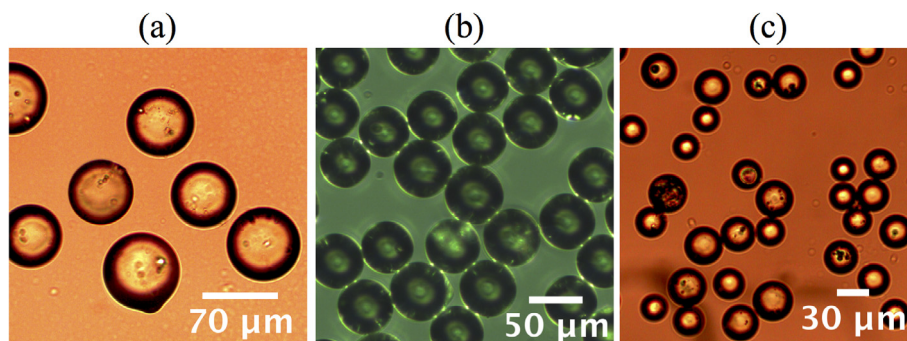
Fig. 1. Microscope images of (a) 69 μm, (b) 49 μm and (c) 29 μm glass spheres.

Table 1
Properties of particles used in experiments.

Diameter range (μm)	Mean diameter, d_p (μm)	Sphericity, ϕ
63–75	69	0.95
45–73	49	0.96
20–38	29	0.95

glass microscope slip (Fig. 2f). Performing sliding friction measurements using a sled removes the ability of the particles to roll, thereby isolating sliding friction. The block on which the sled sits rotates until it is large enough to induce sliding. The static friction coefficient can be determined from the angle of the block at which the sled begins to move. To measure the kinetic friction, the acceleration of the sled down the inclined block is necessary. Accordingly, a high-speed camera is used to record the sled as it slides down a flat piece of material. A soda-lime glass microscope slide was used for the particle-particle friction measurement and an acrylic Plexiglas slab for particle-wall measurements. All friction measurements are performed in a sealable acrylic box in order to remove small air currents from affecting the motion of the sled as well as to control the humidity of the experiments. The friction measurements reported below were made in relative humidity < 5%.

The material properties shared by all particles (friction coefficients, particle density, etc.) in this work are provided in Table 2. It is worthwhile to note that the value of particle-particle e measured here (Table 2) compares well to the commonly used value of 0.97 for soda-lime glass measured by Foerster et al. [63].

2.1.2. Particle surface roughness: SEM vs. AFM

As mentioned previously, the cohesion magnitude is relevant to fluidization behavior in addition to the particle and material properties reported above. The mild cohesion of the Group A particles used in this work is caused by van der Waals forces, which are strongly influenced by surface roughness. As mentioned in the Introduction, SEM images illustrate the qualitative nature of asperities on a surface, but do not provide adequate quantitative information. Nonetheless, SEM images are commonly reported in lieu of the more quantitative AFM surface roughness measurements. To highlight the differences between the two methods and demonstrate the need for AFM surface roughness measurements, here we include measurements of the surface roughness using both SEM and AFM. A JEOL JSM-7401F Field Emission SEM was used for the SEM images acquired for this work. The surface roughness was mapped using a Dimension Edge AFM from Bruker using PeakForce Tapping™ model (further details are provided in [47]). Using AFM, the surface roughness was measured on 6 particles from each size range.
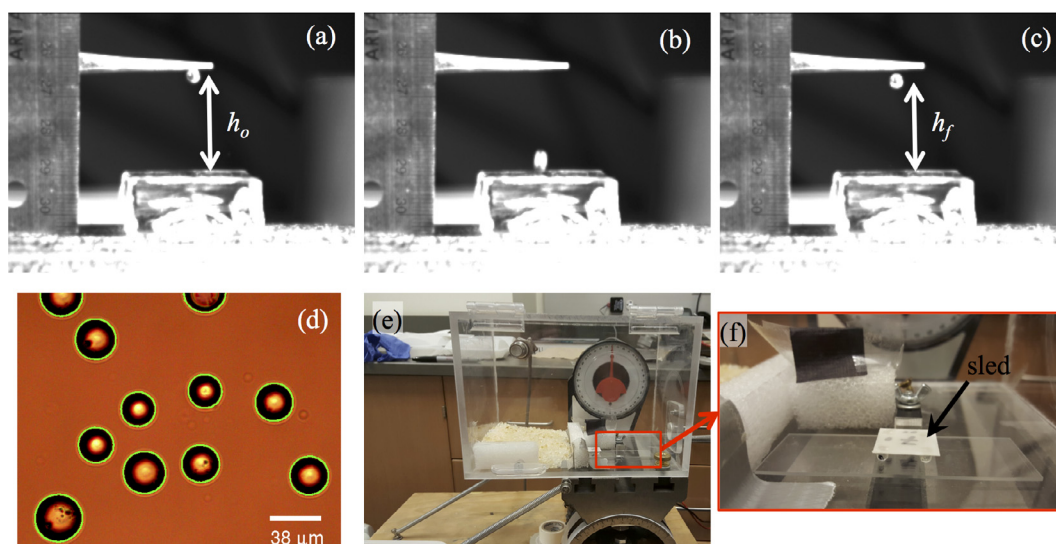

Fig. 2. Images to overview cost effective ways of measuring particle properties: (a–c) coefficient of restitution where the particle is at h_o in (a), impacting the plate in (b) and at h_f in (c), (d) sphericity where the green lines trace the detected perimeters of the particles imaged with an optical microscope, (e) device for measuring the coefficient of friction and (f) the sled used to measure coefficient of friction (zoomed in from (e)). (For interpretation of the references to color in this figure legend, the reader is referred to the web version of this article.)

Table 2
Material properties (same for all particles used in this study).

Property	Value
Particle-particle kinetic friction coefficient [62], μ_k	0.273 ± 0.02
Particle-wall kinetic friction coefficient, μ_{kw}	0.25 ± 0.03
Particle-particle static friction coefficient, μ_s	0.358 ± 0.008
Intrinsic density, ρ_p (kg/m^3)	2500
Hamaker constant [64], A (J)	3.1×10^{-20}
Coefficient of restitution, e	0.970 ± 0.006
Particle-wall coefficient of restitution, e_w	0.955 ± 0.005

SEM provides a two-dimensional image with very high lateral resolution, but there is no quantified link between SEM pixel intensity and asperity height (the third dimension) [45]. Conversely, AFM provides a three-dimensional topographical map of the surface resulting in detailed quantitative measurements of surface roughness with nanometer scale resolution in lateral direction and sub-nanometer in height. Fig. 3a-c contains such AFM maps for the particles used in this work. The lack of quantitative values for roughness height from SEM images is illustrated in Fig. 3d by applying the method presented by Marinello et al. [45] to the particles used in this work. More specifically, the pixel intensities from an SEM image across the centerline of a spherical particle are compared to the expected curvature of the particle (neglecting roughness). Fig. 3d provides an SEM image of a particle from the 20–38 µm size range with a blue line drawn across the centerline of the particle. The topographical profile along the centerline of the spherical particle is expected to follow a semicircular arc, as drawn in Fig. 3e (red dashed line). However, plotting the pixel intensities of the SEM image taken along the centerline (blue line in Fig. 3e) does not recover the expected semicircular height profile. (See Ref. [45] for a discussion on possibilities of measuring surface topography using stereoscopic SEM and the associated limitations.)

2.1.3. Determining van der Waals force From AFM measurements

AFM can be used to measure particle roughness, as detailed above, and/or forces between particles, which is illustrated in

Fig. 4. The former measurement (Fig. 4a-c) is fairly straightforward, whereas the latter involves subtleties that cannot easily be overcome in order to obtain cohesive force vs. separation distance. More specifically, a measurement of the "pull-off force" (adhesion force), or force required to separate two surfaces in contact (Fig. 4d), is possible via AFM, but non-contact forces (when surfaces are separated by small, but nonzero distances) are difficult to resolve [65]. Moreover, to obtain a "clean" measure of the pull-off force between two particles, the particle glued to the tip of the AFM cantilever must contact the particle glued to the substrate such that a normal (non-oblique) contact occurs between the surfaces; otherwise, a frictional contact will result and thus add, in a manner that is difficult to quantify [66], to the normal force. For non-spherical particles, the aforementioned situation is further complicated. Accordingly, making measurements of surface roughness on several particles, and then using analytical [40,47,53,67] or numerical methods (e.g. summing the van der Waals force between adjacent points on surfaces reconstructed as discretized meshes) [56–58,60,68] to predict the cohesive interaction between particles is more straightforward.

Rabinovich et al. [40,67] developed the commonly used (single-equation) analytical theory for predicting the van der Waals force between one hard, rough surface and one hard, smooth surface by modifying the Hamaker theory to account for roughness as submerged-spherical asperities. The roughness on the surfaces studied by Rabinovich [40] were classified into two types, namely, roughness that can be considered as a single scale, and roughness that can be modeled as two superimposed scales (small- and large-scale roughness). The latter classification is appropriate for the particles used here, as discussed below (Fig. 4c). Accordingly, to characterize the roughness such that it can be used as inputs to standard van der Waals force models (e.g. [67]), the roughness measured in these AFM surface maps is separated into small- and large-scale contributions via high- and low-pass fast Fourier transform filters [47]. Next, the roughness wavelength and amplitude of each scale is characterized by a mean wavelength (λ_i) and root mean square height (rms_i) [47], the process for which is summarized in Fig. 4a-c (details available elsewhere [47]). Fig. 4c
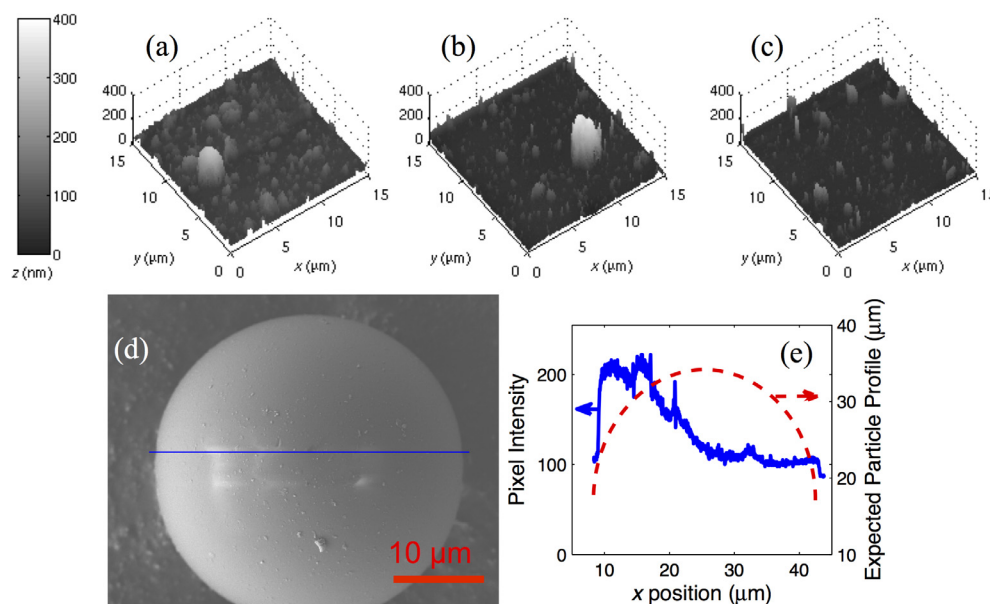

Fig. 3. AFM images of surfaces of (a) 69 µm, (b) 49 µm and (c) 29 µm glass spheres. (d) SEM image of a surface of a 29 µm glass sphere, and (e) the corresponding line trace of pixel intensities along the blue line in (d) from left to right compared to the height profile expected along the centerline of the particle assuming the particle is perfectly spherical. The edge of the particle in (d) is approximately 8 µm from the edge of the image, which is reflected in x position pixel intensity and expected particle curvature plotted in (e). (For interpretation of the references to color in this figure legend, the reader is referred to the web version of this article.)
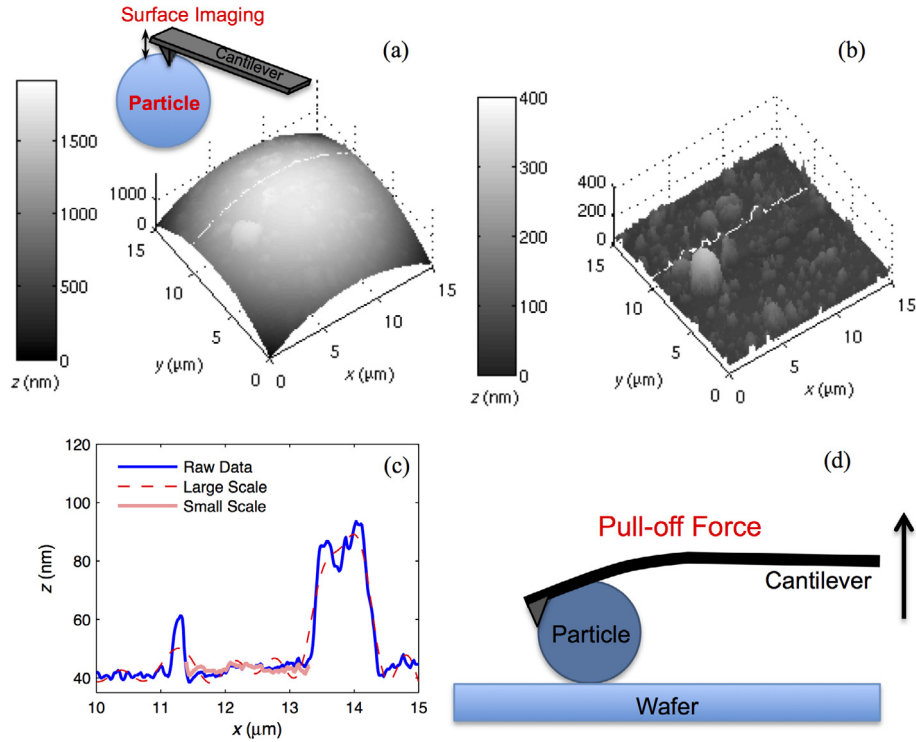
Fig. 4. (a) AFM surface mapping of a particle surface (inset is a schematic of the AFM tip scanning the surface of the particle), (b) the AFM surface map in (a) with the background particle curvature subtracted, (c) the surface roughness separated into large- and small-scale components for one line on the surface, and (d) schematic of the van der Waals force measurement.

exemplifies that two superimposed roughness scales can classify the surface roughness of the particles used here. Rabinovich et al. [40] originally advocated separating surface roughness into two scales, as they found the small-scale roughness determined the pull-off force. However, large-scale surface roughness is still important at larger separation distances (unlike the pull-off force which is measured for the particles in contact). The methodology summarized here to separate and characterize surface roughness is validated and explained in detail elsewhere [47]. Table 3 provides surface roughness parameters of the particles used here [47].

To demonstrate the role of cohesion on the measured fluidization behavior, predictions of the maximum van der Waals force, or adhesion force, $F_{c,m}$, is also provided in Table 3. $F_{c,m}$ was determined using the modified Rabinovich et al. model given by [40,47],

[40,67]. Liu et al. [6,15] validated the van der Waals force model (Eq. (1) applied to all separation distances, $D \geqslant D_o$) by comparing DEM predictions of defluidization curves to experimental data. The predicted adhesion forces (Table 3) are similar magnitudes for all particle sizes because the surface roughness is similar for all of the particles. Thus, for the parameter range studied here, the effects of roughness dominate cohesion over particle size, demonstrating the importance of measuring surface roughness for cohesive particles. To illustrate the increasing role of cohesion as the particle size decreases, Table 3 also provides the ratio of the maximum van der Waals force between particles to the particle weight ($w_p \propto d_p^3$), or Bond number (Bo). With increasing particle size, the maximum cohesive force increases with particle diameter if the particles are perfectly smooth ($F_{c,m} \propto d_p$) and Bo would

$$F_{c,m} = \frac{A}{6}\left[\frac{R}{2(D_o + 2z_l + 2z_s)^2} + \frac{2Rr_l}{(R + r_l)(D_o + z_l + 2z_s)^2} + \frac{2Rr_s}{(R + r_s)(D_o + z_l + z_s)^2} + \frac{r_l}{2(D_o + 2z_s)^2} + \frac{2r_lr_s}{(r_l + r_s)(D_o + z_s)^2} + \frac{r_s}{2D_o^2}\right] \quad (1)$$

where A is the Hamaker constant (Table 2), R is the particle radius ($d_p/2$), D_o is the minimum separation distance ($D_o = 0.3$ nm is used for particles in contact to avoid an infinite force prediction [40]), r_i and z_i are the asperity radius and height for scale i (i is either large (l) or small (s) scale). The asperity radius and height are related to the measured roughness parameters (λ_i and rms_i; Table 3) by $r_i = \frac{\lambda_i^2}{32k_1 rms_i}$ and $z_i = k_1 rms_i$ where the coefficient $k_1 = 1.817$

decrease accordingly ($Bo \propto d_p^{-2}$). However, the cohesive force between the particles used here is determined by surface roughness and independent of d_p, and therefore $Bo \propto d_p^{-3}$ (see Table 3). It is worthwhile to note that variation in the measured surface roughness between particles leads to cohesion force magnitudes that vary across particle sizes. Therefore, in reality, Bo is only approximately proportional to d_p^{-3}.

Table 3
Properties related to van der Waals cohesion of particles used in experiments.

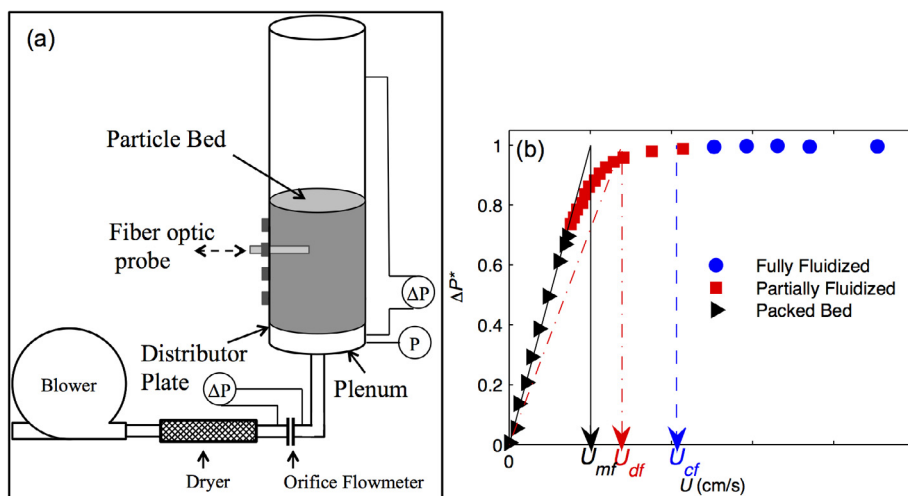| Diameter range (μm)	Roughness parameters [47]				Predicted particle-particle maximum force, $F_{c,m}$ (nN)	Bond Number, Bo
	Large-scale		Small-scale			
	λ_l (nm)	rms_l (nm)	λ_s (nm)	rms_s (nm)		
63–75	2400 ± 400	24 ± 8	300 ± 100	2 ± 1	18	7
45–73	2600 ± 700	45 ± 40	260 ± 20	1.8 ± 0.6	20	13
20–38	1800 ± 500	30 ± 20	300 ± 60	1.4 ± 0.2	28	57

Fig. 5. (a) Fluidized bed apparatus used for experiments. (b) Definition of characteristic velocities U_{mf}, U_{df} and U_{cf} taken from the defluidization pressure drop vs. gas velocity curve. (For interpretation to colours in this figure, the reader is referred to the web version of this paper.)

2.2. Fluidized bed apparatus

Experiments were performed in a fluidized bed, which is schematized in Fig. 5a. The fluidized bed is composed of a Plexiglas cylinder with an inner diameter of 18.4 cm. A Fuji regenerative blower supplied air at local atmospheric conditions (density 0.97 kg/m³, and viscosity 1.83×10^{-5} Pa s) to the bottom of the bed. A Lambda-square 4150-P orifice plate (with bore size 1.213 cm) was used to measure the air flow rate to the bed. A sintered stainless steel porous plate with average porosity of 5 μm from Mott Corp. was used to distribute gas uniformly to the bottom of the bed. Uniform gas distribution was ensured as the pressure drop across the distributor plate was always > 0.2 times the pressure drop across the bed [69]. Pressures were measured using Halstrup Walcher pressure transducers with accuracy of 0.2%. The relative humidity (measured using an Omega HX93AV-RP1 hygrometer with accuracy ± 2.5% between 20% and 80% and 3.1% in extreme humidity levels) was held below 5% for all experiments in order to remove the effects of humidity, as it was previously found that the defluidization curve obtained for the same 63–75 μm glass particles used here was sensitive to relative humidity levels >10% [62]. Electrostatics were minimized using a copper wire wrapped around the outside of the column and a metal base, and antistatic spray – Kensington Dust Guardian – applied to the walls of the column. Further details of the fluidized bed are provided elsewhere [37,62,70].

In addition to carefully characterizing particles, a detailed protocol was followed for fluidized-bed experiments to ensure repeatability of measurements. For instance, defluidization was always performed before fluidization, to ensure a consistent solids volume fraction at the onset of fluidization. To initialize the bed for defluidization experiments, the gas velocity was held at a maximum value (depended on particle size) that was high enough to ensure the bed was fully fluidized and bubbling. The velocity was

held at the maximum value for at least 20 min after the relative humidity dropped below 1%. The gas velocity, U, was decreased incrementally, and the pressure drop across the bed, ΔP, was measured at each successive velocity setting. The velocity was held constant for 60 s after each change, and only the last 40 s of velocity and pressure drop measurements were recorded to ensure the flow through the bed had reached steady state. Once U reached zero flow, fluidization ensued by successive increases in the gas velocity until the max U was reached, similarly measuring ΔP at each constant U setting. Measurements were recorded at 60 Hz. At least 6 trials were repeated. Fig. 5b presents an example defluidization curve – i.e. ΔP^* vs. U, where ΔP^* is the pressure drop across the bed normalized by the bed weight (W_b) over the cross sectional area (A_b) of the column, $\Delta P^* = \Delta P A_b/W_b$. Additionally, Fig. 5b illustrates the definition of the velocities used to characterize the defluidization curve: minimum fluidization velocity (U_{mf}), minimum defluidization velocity (U_{df}), and complete fluidization velocity (U_{cf}). U_{mf} is defined using the classic method of Richardson [71], in which the packed-bed portion of the defluidization curve (black triangles) is fit to a linear least squares fit and the intersection with $\Delta P^* = 1$. U_{cf} was originally developed to describe the onset of defluidization in polydisperse flows [70,72] and is the first point in the defluidization curve where the drag force no longer matches the particle weight, i.e. the first point with $\Delta P^* < 1$ (threshold used here $\Delta P^* = 0.98$). U_{df} is similar to U_{cf} in that it incorporates the region of partial fluidization, but similar to U_{mf} in that it is defined by the intersection of a linear fit of all points not fluidized (both partially fluidized and packed bed instead of just packed bed) with $\Delta P^* = 1$. All characteristic velocities U_{mf}, U_{df} U_{cf}, and U_{mb} (defined below) are reported in the Results and Discussion section for the sake of completeness [15,33].

The surface of the bed is tracked through the clear wall of the column in order to measure the bed height, H_b. From H_b, the bed
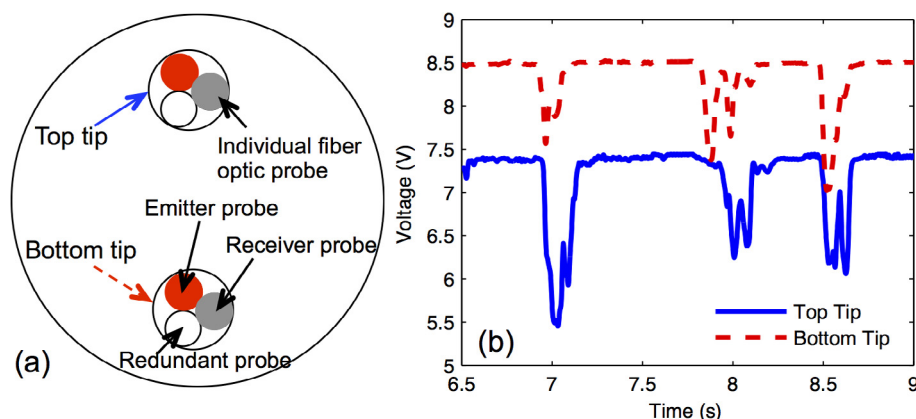
Fig. 6. (a) Fiber optic based bubble probe used to detect bubbles and (b) voltage traces from the fiber optic probe.

mass (M_b) and solids density (ρ_p, Table 2), the average solid volume fraction (ε_s) can be determined. The bed mass was always 6 kg for defluidization experiments (a larger mass was used for the bubble probe experiments discussed below), unless otherwise stated. H_b measurements are also used to determine U_{mb} [69], which is the incipient bubbling velocity, as the velocity at which fluctuations in the bed surface (and thus H_b) begin during fluidization or cease during defluidization. Using fluctuations in H_b to determine U_{mb} coincides with visual observations of the onset (or cessation) of bubbles in the bed that erupt at the surface [73], except for the occasional bubble that would be observed for U below U_{mb}.

As Fig. 5a illustrates, several ports are located axially up the column, in which the fiber-optic probe used to measure bubble properties can be inserted. The bubble probe is composed of two sets of fiber optic wires, namely a top and bottom tip. As illustrated in Fig. 6a, each tip is composed of a source, a receiver and a redundant wire. The source wire is connected to an LED with a controlled intensity. The receiver wire connects to a photodiode that turns the received light into a measureable voltage signal. In the presence of the emulsion (high concentration of particles), much of the light emitted from the source wire is reflected back to the receiver wire, and a high voltage is measured. However, in the presence of a bubble, or void, less light is reflected back to the receiver wire, resulting in a smaller voltage relative to the presence of the emulsion. As a bubble moves up the bed it first passes the bottom tip and then the top tip, resulting in a voltage drop measured by both tips, as demonstrated in Fig. 6b. The top and bottom tip signals are recorded at 1000 Hz for 30 s segments, and the voltage drops used to determine the bubble diameter or pierce/chord length (D_{bub}), frequency (f_{bub}) and vertical velocity (V_{bub}) with the method of Chew and Hrenya [37], which is similar to past works with bubble probes [25]. Minor differences in the analysis algorithm implemented by Chew and Hrenya [37] to the one instituted here were used. First, electrical noise is filtered from the optic probe signal by removing everything with a frequency >60 Hz. Similar to [37], the bubbles are distinguished from the emulsion using a threshold voltage. Each continuous voltage drop below the threshold is considered a bubble and f_{bub} is determined by counting the number of bubbles in the measurement time. The time lag between bubble appearances in the bottom and top probe is determined using the cross-correlation of the two signals, namely the average time lag is taken as the time shift that results in the strongest correlation between the signals. V_{bub} is determined from the time lag and the measured distance between tips, namely 0.25 cm. V_{bub} and the time taken by individual bubbles to pass a tip (the duration of each voltage drop below the threshold) are used to determine D_{bub}. To use all bubble probe ports available on the column, a bed mass of 9.1 kg was used for bubble characterization experiments.

3. Results and discussion

The defluidization and bubble results are separated below, since defluidization is system-size independent [15,33], but bubble properties are not [74]. Using metrics that are insensitive to system-size allows for models to be validated by comparing small-scale simulations with large-scale experiments [15,33]. Therefore, defluidization can be used to validate both continuum (where the experimental system size can be matched) and DEM (where the number of particles that can be simulated is limited to orders of magnitude less than present in the experiments) models. However, because bubble properties are system-size dependent, they can be used to validate continuum models but not DEM due to the size of the experimental system used here ($\sim O(10^{10}$–$10^{11})$ particles).

3.1. Defluidization curves

As particle size decreases, particles remain fluidized at smaller velocities. Fig. 7 presents the ΔP^* vs. U defluidization curves for the three particle sizes considered here. LaMarche et al. [62] showed cohesive particles exhibit a partially fluidized region where the bed compacts with decreasing gas velocity, resulting in a non-linear region of the defluidization (ΔP^* vs. U) curve. The dashed lines in Fig. 7 are the linear fits of the packed bed region extrapolated to $\Delta P^* = 1$ (i.e. black line to extrapolate U_{mf} in Fig. 5b), which helps illustrate the increasing partially-fluidized region as d_p
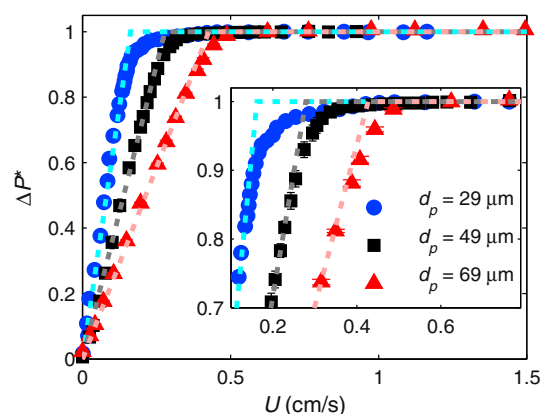

Fig. 7. Defluidization curves (ΔP^* vs. U) for three particle sizes; the light colored dashed lines are a linear fit of the packed bed region intersecting with $\Delta P^* = 1$ and are intended to guide the eye. Error bars represent 95% confidence intervals, but are often too small to see on the scale of the plot.
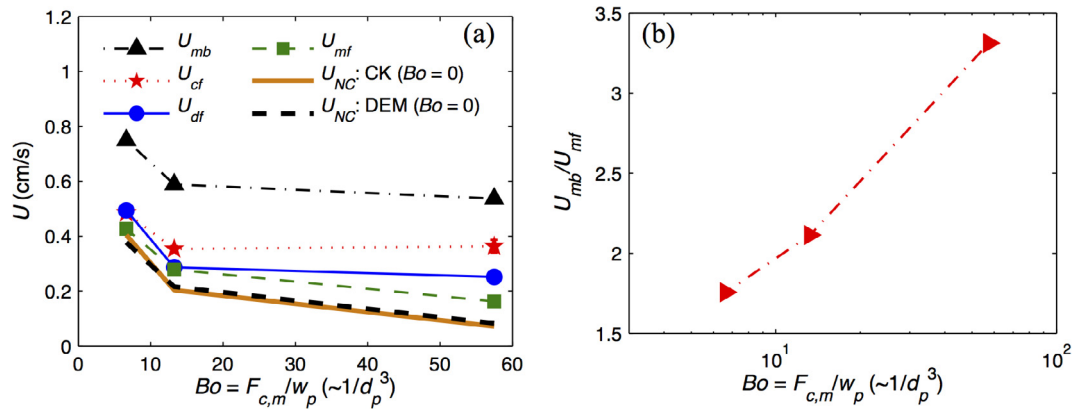
Fig. 8. (a) Characteristic velocities U_{mf}, U_{df}, U_{cf} and U_{mb} measured with respect to defluidization as well as U_{NC} calculations and (b) the ratio of U_{mb} to U_{mf} for increasing Bo (decreasing d_p). Error bars represent 95% confidence intervals, but are often too small to distinguish on the scale of the plot (i.e., error bars are smaller than the data makers).

decreases. In other words, the relative impact of cohesion increases as particle size decreases, as evidenced by the increasing Bo in Table 3.

This effect of increasing Bo (i.e. increasing cohesion effects) on the defluidization curve is demonstrated quantitatively in Fig. 8. In particular, the increased size of the partially-fluidized region and the corresponding decreasing fluidization velocities (U_{mf}, U_{df} U_{cf}, and U_{mb}) are shown in Fig. 8a as a function of Bo. All characteristic velocities decrease with increasing Bo (except U_{cf} for Bo = 57), but the rate of reduction decreases as Bo increases. For non-cohesive (Group B), monodisperse particles, the characteristic velocities are approximately equal ($U_{mf} \approx U_{mb} \approx U_{df} \approx U_{cf}$) [75] and thus the effects of increasing cohesion on the bed behavior is quantified by the difference between these characteristic velocities and non-cohesive calculations of minimum fluidization velocity U_{NC}, which are included in Fig. 8a. U_{NC} was calculated using two methods: with the Carman-Kozeny (CK) [76] pressure drop correlation using ε_s = 0.58 for all d_p (represents the non-cohesive ε_s) to find the U that corresponds to $\Delta P = W_b/A_b$, and the minimum deflu-idization velocity of the defluidization curve predicted using non-cohesive DEM simulations (using the DEM formulation described elsewhere [15,33]). The sensitivity of the characteristic velocities to cohesion is demonstrated by the difference between the measured value and U_{NC}, and Fig. 8a shows U_{mf} is the least sensitive to increasing cohesion, followed by U_{df}, U_{cf} then U_{mb}. The character-istic velocities increase with Bo relative to U_{NC} because particle

collisions become more dissipative as Bo increases, i.e., particles settle at a larger U than if no cohesion was present. While U_{mb} decreases with increasing Bo (decreasing d_p; Fig. 8a), the ratio U_{mb}/U_{mf} increases as Bo increases (Fig. 8b) due to the increasing role of cohesion as d_p decreases (i.e. as Bo increases particles are closer to Group C classification). Fig. 8b illustrates a logarithmic dependence of U_{mb}/U_{mf} on Bo calculated using Eq. (1). Previous studies using Group C particles found similar dependences on Bo, e.g., $U_{mb} \propto \log(Bo)$ [60], and characteristic velocities similar to $U_{mb} - U_{mf} \propto \log(Bo)$ [77].

Similar to Fig. 8, Fig. 9 provides the effect of increasing Bo as well as bed mass on ε_s. Experimentally it is known that bed expan-sion increases (i.e., ε_s decreases) with increasing Bo (e.g. Refs [73,77,78]), which is also observed in this work (Fig. 9a). The solids volume fraction decreases as d_p decreases because the cohesive magnitude is relatively constant for all particle sizes (Table 3), but the particle mass, which affects Bo (relevant to static bed) and inertia (relevant to the dynamic bed), decreases with decreas-ing d_p. The same qualitative trend in ε_s measured during defluidiza-tion and fluidization is observed for all particle sizes, as illustrated in Fig. 9a. At small U, when the bed is static, a constant ε_s is mea-sured for both fluidization and defluidization, but the static bed persists for a larger range of U for fluidization. At moderate U, ε_s reaches a minimum ($U = U_{mb}$; indicated by the green arrows). For U above U_{mb}, ε_s increases as bubbling increases. The bed undergoes homogenous expansion for both fluidization and defluidization,
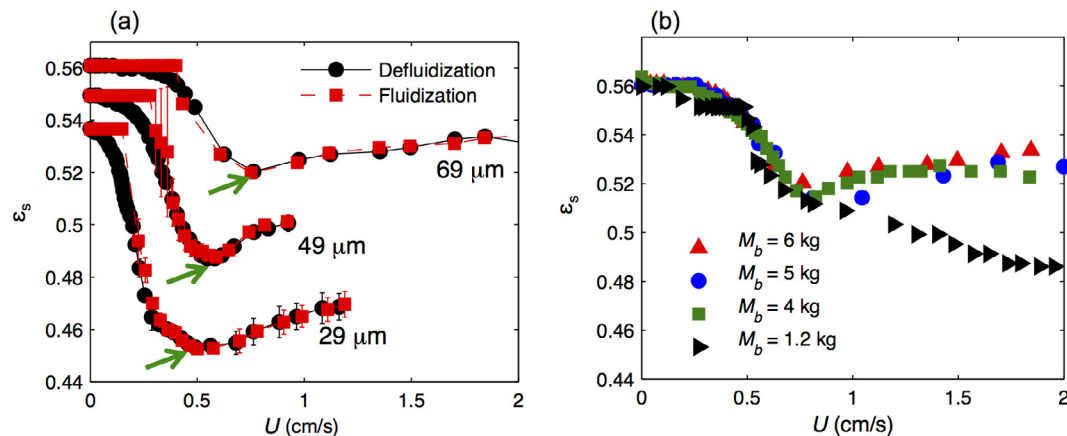

Fig. 9. (a) ε_s vs. U for the three particle sizes with defluidization and fluidization differentiated; the green arrow indicates U_{mb}. (b) ε_s vs. U for d_p = 69 μm particle with varied bed mass for defluidization. Error bars represent 95% confidence intervals. (For interpretation of the references to color in this figure legend, the reader is referred to the web version of this article.)

which occurs for U between the packed-bed region (ε_s = constant; occurs between ~0.1 and 0.4 cm/s for the various particle sizes) and U_{mb} (ε_s = minimum [69]). Hysteresis in ε_s is observed between the defluidization (black circles) and fluidization (red squares) for small U, which corresponds to the partially fluidized region that is a result of increased interparticle forces (higher friction caused by cohesion) that resist compaction of the bed as the gas velocity is lowered (further explained elsewhere [62,79]). As Bo increases (d_p decreases), the range of U for which hysteresis occurs increases.

Previously, the defluidization curve (ΔP^* vs. U, as given in Fig. 8) was identified as a measurement that is independent of system size, allowing for validation of small-scale DEM simulations using large-scale experiments [15,33]. Here, homogenous bed expansion and packed-bed porosity (for $U < U_{mb}$) during defluidization is determined to be another system-size independent measurement, as illustrated in Fig. 9b where ε_s vs. U is presented for beds of the 69 μm particle with varied M_b. In particular, for $U < U_{mb}$ ~0.75 cm/s, the bed expansion (ε_s vs. U) behaves relatively consistently as M_b is reduced, with the exception of small deviations for the smallest bed at $U \sim 0.2$–0.5 cm/s; this deviation is a result of visual distortion of the bed surfaces as it crosses below the top edge of the flange at the bottom of the bed. It is important to note that uniform gas distribution was required for bed expansion (and ΔP^* vs U curve) to be system-size independent (not shown for the sake of brevity). However, only the (homogeneous) bed expansion during defluidization (i.e., $U < U_{mb}$) for the three larger beds does the system-size independent behavior of ε_s extend to $U > U_{mb}$, since ε_s for the smallest bed (M_b = 1.2 kg) does not show a minimum at $U = U_{mb}$, which is likely a result of the comparable bubble size and bed height (similar to slugs formation in tall beds when the bubble size is comparable to column diameter). The mismatch in ε_s vs. U between larger and smallest beds provides an explanation for the difference in bed expansion typically observed experimentally for Group A particles (generally large beds; ε_s reaches a minimum at $U = U_{mb}$, above which ε_s increases) [69,77–81] and in DEM predictions (generally significantly smaller than experiments; ε_s does not reach a minimum) [16,82–84]. Further investigation may provide detailed insight into why ε_s reaches a minimum at U_{mb} for sufficiently high beds. Hence, the homogenous bed expansion and packed-bed porosity measured during defluidization (i.e., $U < U_{mb}$) can be used for comparing small-scale DEM simulations to large-scale experiments. The combination of results in Fig. 8, Fig. 9 and careful characterization of the particles including cohesion (Tables 1–3) allows for a novel, unique data set that can be used to validate cohesion models.

3.2. Bubble properties

Bubbling bed behavior is important for fluidized-bed processes as the bubbles promote mixing [69], and therefore understanding the effects of cohesion on bubble behavior is necessary for optimizing such processes. Some prior work has been done in this regard. For instance, Horio and Nonaka [85] developed a bubble diameter correlation for Group A particles that considers bubble splitting as well as bubble coalescence, as bubble splitting is negligible for non-cohesive particles [85]. Additionally, fluidized beds of both Group B [28,74,86] and Group A particles [19,74] have shown bubbles flow in an annular profiles (bubbles flow faster in the annular region, and slower at the center and the walls). Many of the previous studies on bubble flow did not report detailed particle characteristics (exceptions exist, e.g., Norouzi et al. [86] provided e and μ_k values used in their simulations), and the works investigating Group A particles focused on particles with mean diameters >40 μm. Here, radial and axial profiles of bubble properties are measured for carefully-characterized, Group A particles with particle size down to the 20–38 μm range, thus providing bubble

measurements for (Group A) particles closer to the Group C boundary than previously reported for glass spheres.

The bubble velocity, bubble frequency and bubble diameter for the 69 μm glass particle (Bo = 7) at various radial (r/R) positions are plotted in Fig. 10. For constant U and increasing axial position, h_p, Fig. 10 an illustrates V_{bub}, f_{bub} and D_{bub} are small near the walls and at the center, but increase between the walls and center indicating bubbles flow preferentially in an annulus. Additionally, Fig. 10a shows the bubble characteristics are relatively axisymmetric. In Fig. 10b, V_{bub}, f_{bub} and D_{bub} are compared at various U, but constant h_p. The measurements rendered in Fig. 10b show a statistically significant increase in V_{bub} and D_{bub} from the smallest to largest U value, but no significant change can be identified between the two higher U values. Fig. 10b also illustrates that f_{bub} is relatively insensitive to the range of increased U. Except for f_{bub} measured with the smallest U, the annular bubble flow is observed for increasing U. The reduced bubble flow along the centerline was previously observed by Werther and Molerus [74] to occur in shallow beds (like the bed considered here). Specifically, based on their experimental results with sand, copper powder and glass, with mean d_p larger than ~50 μm, Werther and Molerus [74] found that bubbles preferentially form near the walls of the bed (when porous distributor plates are used), and coalesce and move towards the centerline as they rise. Hence, for shallow beds, bubbles flow in an annulus, and particles recirculate down the centerline of the bed and along the walls. However, for tall beds (taller than two bed diameters [74]), bubbles again form near the wall and initially flow up the annulus, but coalesce and flow preferentially up the center, leading to slugging for very tall beds [31,74]. Similar to Werther and Molerus [74], in this work annular flow refers to an increase in any of the bubble characteristics (i.e. f_{bub}, V_{bub} and/or D_{bub}).

Fig. 11 provides similar information to Fig. 10, but for the more cohesive 49 μm particles (Bo = 13). In particular, at constant U (Fig. 11a), and for h_p values above the smallest axial position (h_p = 12.7 cm), V_{bub} and f_{bub} indicate bubbles flow faster and more frequently in the annular section. For the smallest h_p value in Fig. 11a, V_{bub} is highest for the radial measurements closest to the wall, which agrees with the physical picture presented by Werther and Molerus [74] that bubbles nucleate close to the walls. Furthermore, for $h_p > 12.7$ cm, V_{bub} is smaller for the radial position closest to the walls, but increases with radial positions towards the center, which also agrees with Werther and Molerus [74] that bubbles move inwards, towards the annulus as they move up the column. Moreover, with increasing h_p, f_{bub} values are sustained at the centerline and close to the walls, but increase relative to the smallest h_p in the annular region (this is more clear for $r/R < 0$). Unlike V_{bub} and f_{bub}, D_{bub} does not show an increase in the annular ring and remains relatively constant with increasing h_p, except for the increase in D_{bub} between the bottom two axial positions. Fig. 11b shows that V_{bub} increases with U, but f_{bub} and D_{bub} are relatively insensitive to the range of increased U. Thus bubbles in the 49 μm particle bed behave similar to those in the 69 μm particle bed, with the exception of D_{bub}, which is relatively insensitive to radial position for the 49 μm particle. Furthermore, bubble characteristics for the 49 μm glass are relatively axisymmetric with increasing h_p and U (Fig. 11), which is also similar to the 69 μm glass.

Fig. 12 delineates the behavior of V_{bub}, f_{bub}, and D_{bub} for the most cohesive 29 μm glass particles (Bo = 57). As demonstrated in Fig. 12a, when U is held constant for the smallest size, D_{bub} and f_{bub} are relatively constant for all r/R and h_p, and V_{bub} increases as h_p increases. Additionally, for the smallest particle bed as U is increased (for constant h_p), V_{bub}, D_{bub} and f_{bub} increase near the center of the bed, but the bubble properties near the walls remain relatively constant; see Fig. 12b. Hence, the generalization can be
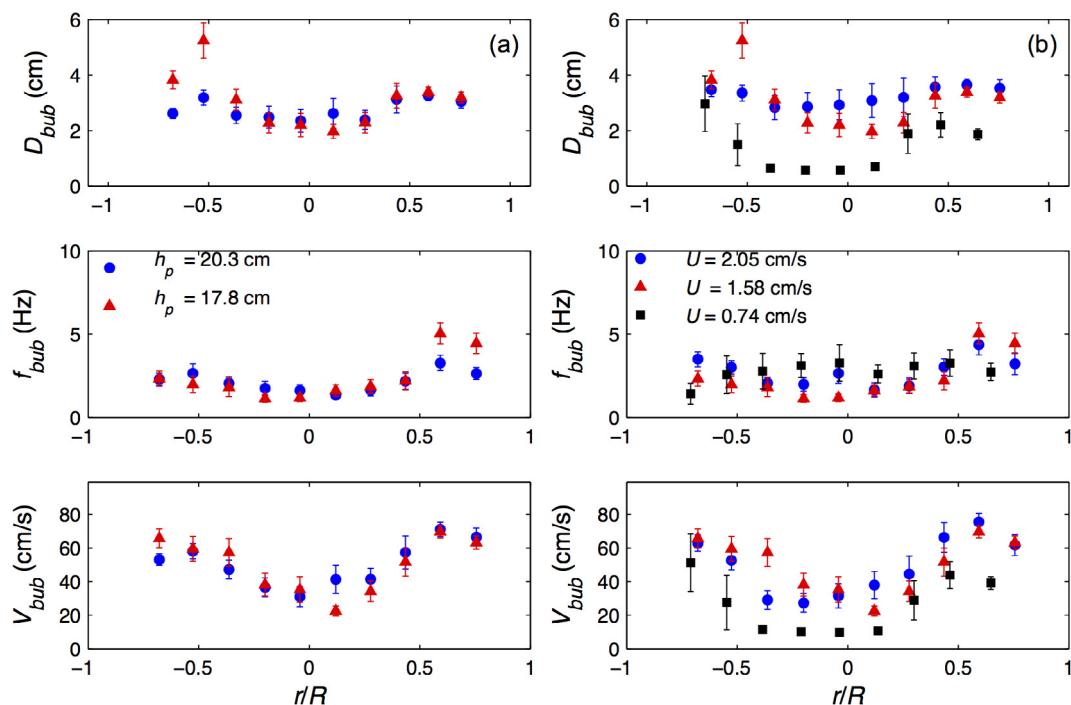
Fig. 10. Radial profiles of bubble diameter, bubble frequency and bubble velocity for 69 μm glass ($Bo = 7$) for (a) $U = 1.86$ cm/s with increasing h_p and (b) constant $h_p = 17.8$ cm and increasing U. Error bars represent 95% confidence intervals.
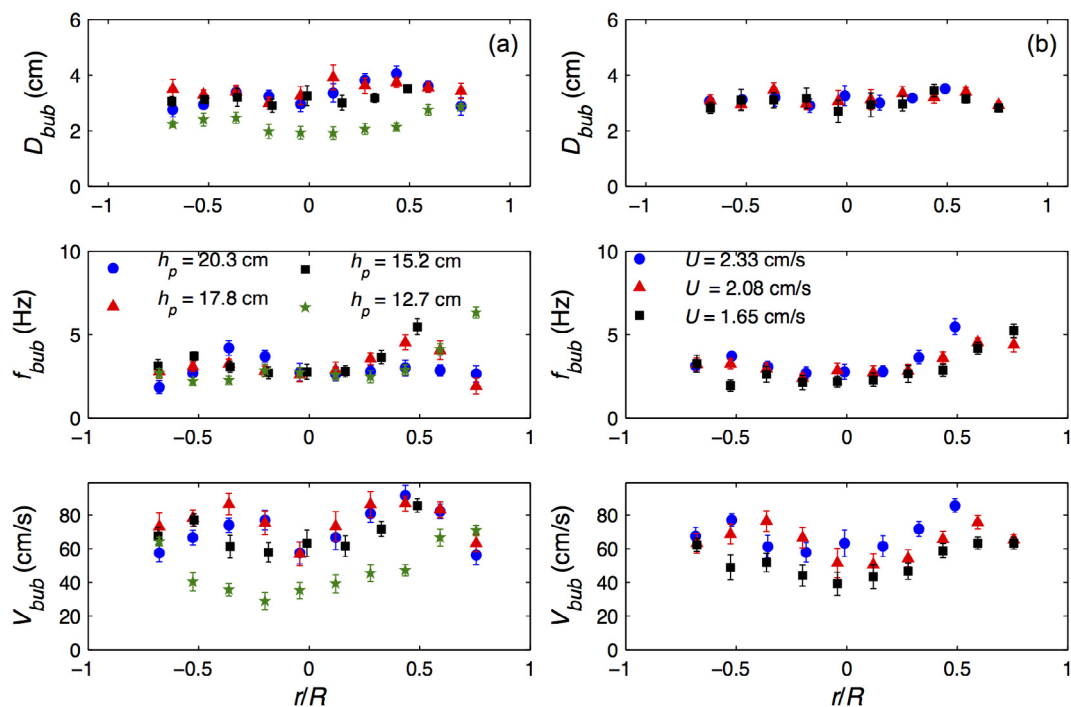

Fig. 11. Radial profiles of bubble diameter, bubble frequency and bubble velocity for 45 μm glass ($Bo = 13$) with (a) $U = 2.33$ cm/s with increasing h_p, and (b) constant $h_p = 15.2$ cm and increasing U. Error bars represent 95% confidence intervals.

made that across all particles sizes, two fairly consistent bubble behaviors observed, (i) the bubble properties are relatively constant near the walls with increasing h_p or U, and (ii) the V_{bub} is generally higher away from the wall. However, unlike the two large particles (less cohesive; Figs. 10 and 11), V_{bub} for the smallest particle does not indicate annular flow, rather it increases uniformly at radial positions away from the walls as h_p or U is increased. Hence,

Fig. 12 illustrates that the annular bubble flow profile is less pronounced for the smallest particle than for the two larger particles (Figs. 10 and 11). Based on the aforementioned physical picture of Werther and Molerus [74], which was formed via experiments using particles with mean diameters >50 μm, the behavior presented in Fig. 12 for the 29 μm glass (flatter profiles) behaves as though it is taller than the beds of 49 μm (Fig. 11) and 69 μm glass
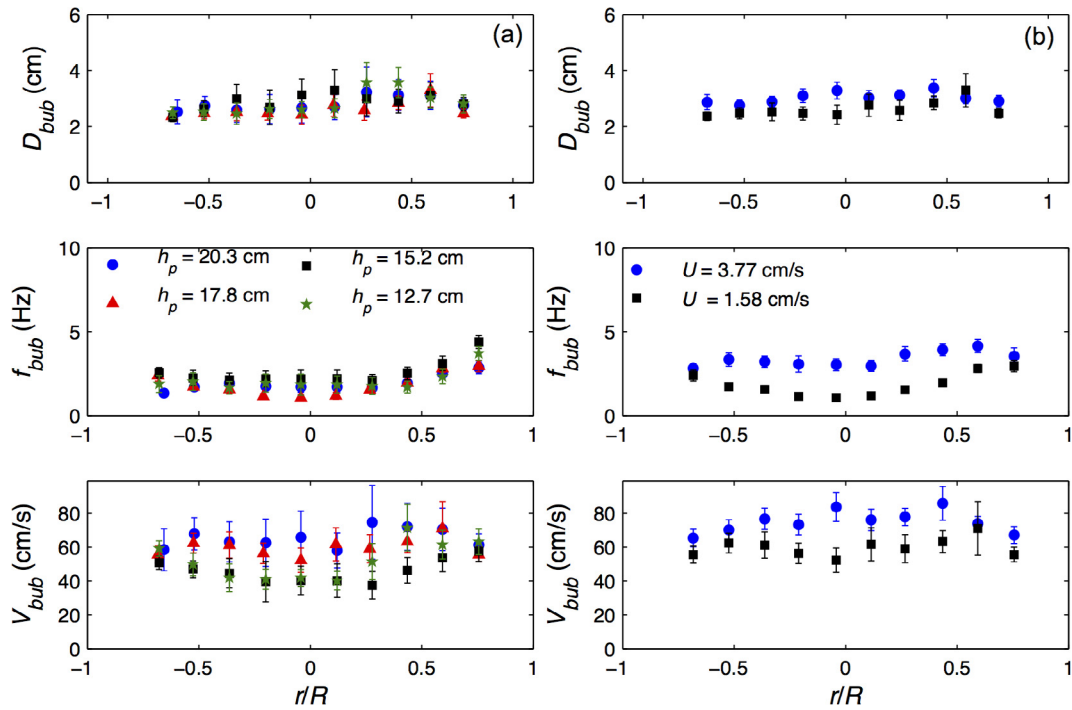
Fig. 12. Radial profiles of bubble diameter, frequency and velocity for 29 μm glass ($Bo = 57$) for (a) $U = 1.58$ cm/s with increasing h_p and (b) constant $h_p = 17.8$ cm and increasing U. Error bars represent 95% confidence intervals.

(Fig. 10). However, the 29 μm glass has only a slightly higher bed height as the same bed mass was used for the three particle types and the higher porosity of the 29 μm glass (extrapolated from Fig. 9). The results presented here indicate annular bubble flow is attenuated as the cohesive nature (i.e. Bo; Table 3) of the particles increases. This may be due to the higher porosity of cohesive particle beds (see Fig. 9 and elsewhere [87]) allowing for more uniform bubble nucleation at the bottom of the bed, thus avoiding the preferential bubble growth at the walls (which is the source of the annular flow profile). Future simulations may provide valuable insight into the underlying physics.

4. Concluding remarks

This work provides fluidization and defluidization measurements and bubble characteristics for well-characterized, mildly cohesive (Group A) particles. Since van der Waals cohesive forces are extremely sensitive to surface roughness, particle surface roughness characterization is provided, for the first time, alongside macroscopic (fluidized-bed) measurements. The partially fluidized region of the defluidization curve increases as particle size decreases (Bo increases). Velocities that characterize the defluidization process (U_{mf}, U_{df}, U_{cf} and U_{mb}) decrease as Bo increases, because the particle weight, and therefore drag required to fluidize the particles, decreases. However, for non-cohesive particles, these characteristic velocities converge to the minimum fluidization velocity (e.g. $U_{mb} = U_{mf}$ for non-cohesive Group B particles), and thus the effects of cohesion (Bo) on fluidization is illustrated by comparing the difference between the measured characteristic velocities and the minimum fluidization velocity calculated by neglecting cohesion, i.e., U_{NC}. This difference between the measured characteristic velocities and the U_{NC} increases as Bo increases, quantitatively demonstrating the increasing effects of cohesion on fluidization behavior as Bo increases. The measured minimum fluidization velocities for the particles are larger than U_{NC} because the packed-bed porosity increases as cohesion

increases. Additionally, the other characteristic velocities (U_{df}, U_{cf}, and U_{mb}), which are measures of the defluidization or settling of particles, are larger than the respective U_{NC} values because particle collisions become more dissipative as cohesion increases (i.e. particles settle, or defluidize, at larger gas velocities than if cohesion was negligible because a larger drag force is required to keep particles in motion). Additionally, bed expansion increases (both in magnitude and duration) as Bo increases. Moreover, bubble characteristics are also reported for the various particles studied. Annular bubble flow profiles [74] are observed for the two larger particle sizes. However, annular bubble flow profiles are not exhibited in bubbling beds of the smallest particle, which has not been reported previously.

The fluidized-bed measurements reported in this work include both system-size independent and system-size dependent measurements. In DEM, the number of particles that can be simulated is largely limited to systems much smaller than lab-scale or industrial units. Accordingly, the system-size independent measurements are particularly useful for assessing the accuracy of DEM models that include van der Waals forces, though can also be used to compare against continuum predictions. The system-size insensitive metrics reported here include defluidization (ΔP^* vs. U) and bed expansion for $U \leqslant U_{mb}$. Conversely, the bubble velocity, frequency, and diameter (chord length) depend on system size, and can thus be used for comparing to continuum predictions only.

To provide the level of detail required for future model validation, measurements were necessary to characterize particle-level properties. Accordingly, straightforward techniques to measure coefficients of friction, coefficient of restitution and shape (sphericity) are described, with the hopes of these measurements being more frequently reported. Detailed characterization of the particle surface roughness via AFM topographical maps is also described; such characterization plays a crucial role in the prediction of van der Waals forces. As with former works, particle density and size are also reported. In sum, this work provides high-fidelity experimental measurements with well-characterized particles that can

be used in future studies to validate continuum and DEM models of mildly cohesive particles.

References

[1] J.S. Curtis, B. van Wachem, Modeling particle-laden flows: a research outlook, AIChE J. 50 (2004) 2638–2645, http://dx.doi.org/10.1002/aic.10394.

[2] Q.F. Hou, Z.Y. Zhou, A.B. Yu, Micromechanical modeling and analysis of different flow regimes in gas fluidization, Chem. Eng. Sci. 84 (2012) 449–468.

[3] Y.C. Zhou, B.H. Xu, A.B. Yu, P. Zulli, An experimental and numerical study of the angle of repose of coarse spheres, Powder Technol. 125 (2002) 45–54.

[4] B. Hoomans, J. Kuipers, W.J. Briels, W. Van Swaaij, Discrete particle simulation of bubble and slug formation in a two-dimensional gas-fluidised bed: a hard-sphere approach, Chem. Eng. Sci. 51 (1996) 99–118.

[5] J.R. Royer, D.J. Evans, L. Oyarte, Q. Guo, E. Kapit, M.E. Möbius, et al., High-speed tracking of rupture and clustering in freely falling granular streams, Nature 459 (2009) 1110–1113, http://dx.doi.org/10.1038/nature08115.

[6] P. Liu, C.Q. LaMarche, K.M. Kellogg, S. Leadley, C.M. Hrenya, Cohesive grains: Bridging microlevel measurements to macrolevel flow behavior via surface roughness, AIChE J. 62 (2016) 3529–3537, http://dx.doi.org/10.1002/aic.15383.

[7] Y. Chen, J. Yang, R.N. Dave, R. Pfeffer, Fluidization of coated group C powders, AIChE J. 54 (2008) 104–121, http://dx.doi.org/10.1002/aic.11368.

[8] Y. Chen, M.A.S. Quintanilla, J. Yang, J.M. Valverde, R.N. Dave, Pull-off force of coated fine powders under small consolidation, Phys. Rev. E. 79 (2009) 041305.

[9] T. Kobayashi, T. Tanaka, N. Shimada, T. Kawaguchi, DEM–CFD analysis of fluidization behavior of Geldart Group A particles using a dynamic adhesion force model, Powder Technol. 248 (2013) 143–152, http://dx.doi.org/10.1016/j.powtec.2013.02.028.

[10] M.A.S. Quintanilla, J.M. Valverde, A. Castellanos, Adhesion force between fine particles with controlled surface properties, AIChE J. 52 (2006) 1715–1728, http://dx.doi.org/10.1002/aic.10770.

[11] J.K. Pandit, X.S. Wang, M.J. Rhodes, A DEM study of bubble formation in Group B fluidized beds with and without cohesive inter-particle forces, Chem. Eng. Sci. 62 (2007) 159–166, http://dx.doi.org/10.1016/j.ces.2006.08.013.

[12] J.K. Pandit, X.S. Wang, M.J. Rhodes, Study of Geldart's group A behaviour using the discrete element method simulation, Powder Technol. 160 (2005) 7–14, http://dx.doi.org/10.1016/j.powtec.2005.04.044.

[13] M.J. Rhodes, X.S. Wang, M. Nguyen, P. Stewart, K. Liffman, Use of discrete element method simulation in studying fluidization characteristics: influence of interparticle force, Chem. Eng. Sci. 56 (2001) 69–76, http://dx.doi.org/10.1016/S0009-2509(00)00427-9.

[14] R.Y. Yang, R.P. Zou, A.B. Yu, Computer simulation of the packing of fine particles, Phys. Rev. E. 62 (2000) 3900–3908.

[15] P. Liu, C.Q. LaMarche, undefined author, K.M. Kellogg, C.M. Hrenya, Fine-particle defluidization: Interaction between cohesion, Young's modulus and static bed height, Chem. Eng. Sci. 145 (2016) 266–278, http://dx.doi.org/10.1016/j.ces.2016.02.024.

[16] J.E. Galvin, S. Benyahia, The effect of cohesive forces on the fluidization of aeratable powders, AIChE J. 60 (2014) 473–484, http://dx.doi.org/10.1002/aic.14307.

[17] M.J.V. Goldschmidt, R. Beetstra, J.A.M. Kuipers, Hydrodynamic modelling of dense gas-fluidised beds: comparison and validation of 3D discrete particle and continuum models, Powder Technol. 142 (2004) 23–47, http://dx.doi.org/10.1016/j.powtec.2004.02.020.

[18] A. Busciglio, G. Vella, G. Micale, L. Rizzuti, Analysis of the bubbling behaviour of 2D gas solid fluidized beds: Part I. Digital image analysis technique, Chem Eng J. 140 (2008) 398–413.

[19] R. Andreux, J. Chaouki, Behaviors of the bubble, cloud, and emulsion phases in a fluidized bed, AIChE J. 54 (2008) 406–414, http://dx.doi.org/10.1002/aic.11390.

[20] T.E. Broadhurst, H.A. Becker, Onset of Fluidization and Slugging in Beds, AIChE J. 21 (1975) 238–247.

[21] G.C. Brouwer, E.C. Wagner, J.R. van Ommen, R.F. Mudde, Effects of pressure and fines content on bubble diameter in a fluidized bed studied using fast X-ray tomography, Chem Eng J. 207–208 (2012) 711–717.

[22] J.M. Burgess, P.H. Calderbank, The measurement of bubble properties in two-phase dispersions—III, Chem. Eng. Sci. 30 (1975) 1511–1518.

[23] A. Busciglio, G. Vella, G. Micale, L. Rizzuti, Experimental analysis of bubble size distributions in 2D gas fluidized beds, Chem. Eng. Sci. 65 (2010) 4782–4791.

[24] M. Goldschmidt, J.M. Link, S. Mellema, J. Kuipers, Digital image analysis measurements of bed expansion and segregation dynamics in dense gas-fluidised beds, Powder Technol. 138 (2003) 135–159.

[25] M. Rüdisüli, T.J. Schildhauer, S.M.A. Biollaz, J.R. van Ommen, Bubble characterization in a fluidized bed by means of optical probes, Int J Multiphase Flow. 41 (2012) 56–67, http://dx.doi.org/10.1016/j.ijmultiphaseflow.2012.01.001.

[26] M. Rüdisüli, T.J. Schildhauer, S.M.A. Biollaz, A. Wokaun, J.R. van Ommen, Comparison of bubble growth obtained from pressure fluctuation measurements to optical probing and literature correlations, Chem. Eng. Sci. 74 (2012) 266–275, http://dx.doi.org/10.1016/j.ces.2012.01.045.

[27] M. Rüdisüli, T.J. Schildhauer, S.M.A. Biollaz, J.R. van Ommen, Radial bubble distribution in a fluidized bed with vertical tubes, Ind Eng Chem Res. 51 (2012) 13815–13824, http://dx.doi.org/10.1021/ie3004418.

[28] C.E.J. van Lare, H.W. Piepers, J.N. Schoonderbeek, D. Thoenes, Investigation on bubble characteristics in a gas fluidized bed, Chem. Eng. Sci. 52 (1997) 829–841, http://dx.doi.org/10.1016/S0009-2509(96)00442-3.

[29] C.R. Müller, S.A. Scott, D.J. Holland, B.C. Clarke, A.J. Sederman, J.S. Dennis, et al., Validation of a discrete element model using magnetic resonance measurements, Particuology 7 (2009) 297–306, http://dx.doi.org/10.1016/j.partic.2009.04.002.

[30] C.R. Müller, D.J. Holland, A.J. Sederman, S.A. Scott, J.S. Dennis, L.F. Gladden, Granular temperature: comparison of magnetic resonance measurements with discrete element model simulations, Powder Technol. 184 (2008) 241–253, http://dx.doi.org/10.1016/j.powtec.2007.11.046.

[31] C.N. Lim, M.A. Gilbertson, A.J.L. Harrison, Bubble distribution and behaviour in bubbling fluidised beds, Chem. Eng. Sci. 62 (2007) 56–69.

[32] R. Beetstra, J. Nijenhuis, N. Ellis, J.R. van Ommen, The influence of the particle size distribution on fluidized bed hydrodynamics using high-throughput experimentation, AIChE J. 55 (2009) 2013–2023, http://dx.doi.org/10.1002/aic.11790.

[33] C.Q. LaMarche, P. Liu, K.M. Kellogg, A.W. Weimer, C.M. Hrenya, A system-size independent validation of CFD-DEM for noncohesive particles, AIChE J. 61 (2015) 4051–4058, http://dx.doi.org/10.1002/aic.15057.

[34] M. Goldschmidt, J. Kuipers, W. Van Swaaij, Hydrodynamic modelling of dense gas-fluidised beds using the kinetic theory of granular flow: effect of coefficient of restitution on bed dynamics, Chem. Eng. Sci. 56 (2001) 571–578.

[35] M. Goldschmidt, R. Beetstra, J. Kuipers, Hydrodynamic modelling of dense gas-fluidised beds: Comparison of the kinetic theory of granular flow with 3D hard-sphere discrete particle simulations, Chem. Eng. Sci. 57 (2002) 2059–2075.

[36] G. Yasui, L.N. Johanson, Characteristics of gas pockets in fluidized beds, AIChE J. 4 (1958) 445–452.

[37] J.W. Chew, C.M. Hrenya, Link between bubbling and segregation patterns in gas-fluidized beds with continuous size distributions, AIChE J. 57 (2011) 3003–3011, http://dx.doi.org/10.1002/aic.12507.

[38] O. Molerus, Interpretation of Geldart's type A, B, C and D powders by taking into account interparticle cohesion forces, Powder Technol. 33 (1982) 81–87, http://dx.doi.org/10.1016/0032-5910(82)85041-9.

[39] J.N. Israelachvili, Intermolecular and Surface Forces, 3rd ed., Academic Press, Boston, 2011.

[40] Y.I. Rabinovich, J.J. Adler, A. Ata, R.K. Singh, B.M. Moudgil, Adhesion between nanoscale rough surfaces II. measurement and comparison with theory, J. Colloid Interface Sci. 232 (2000) 17–24, http://dx.doi.org/10.1006/jcis.2000.7168.

[41] J.R. Royer, E.I. Corwin, A. Flior, M.-L. Cordero, M.L. Rivers, P.J. Eng, et al., Formation of granular jets observed by high-speed X-ray radiography, Nat. Phys. 1 (2005) 164–167, http://dx.doi.org/10.1038/nphys175.

[42] P. Lettieri, D. Newton, J.G. Yates, Homogeneous bed expansion of FCC catalysts, influence of temperature on the parameters of the Richardson–Zaki equation, Powder Technol. 123 (2002) 221–231.

[43] Z. Zou, H.-Z. Li, Q.-S. Zhu, The bubbling behavior of cohesive particles in the 2D fluidized beds, Powder Technol. 212 (2011) 258–266.

[44] Z. Zou, H. Li, Q. Zhu, Y. Wang, Experimental study and numerical simulation of bubbling fluidized beds with fine particles in two and three dimensions, Ind. Eng. Chem. Res. 52 (2013) 11302–11312, http://dx.doi.org/10.1021/ie303105v.

[45] F. Marinello, P. Bariani, E. Savio, A. Horsewell, L. De Chiffre, Critical factors in SEM 3D stereo microscopy, Meas. Sci. Technol. 19 (2008) 065705, http://dx.doi.org/10.1088/0957-0233/19/6/065705.

[46] C.F. Quate, The AFM as a tool for surface imaging, Surf. Sci. 299/300 (1994) 980–995, http://dx.doi.org/10.1016/0039-6028(94)90711-0.

[47] C.Q. LaMarche, S. Leadley, P. Liu, K.M. Kellogg, C.M. Hrenya, Method of quantifying surface roughness for accurate adhesive force predictions, Chem. Eng. Sci. 158 (2017) 140–153, http://dx.doi.org/10.1016/j.ces.2016.09.024.

[48] D. Zhang, X.-Q. Chen, Y. Wang, F.-H. Zhang, Y. Gan, Relationship between asperity-mediated surface forces and topography alteration of silica microspheres sliding on mica, sapphire, and glass substrates under ambient conditions: atomic force microscopy and theoretical studies, Langmuir 30 (2014) 3729–3740, http://dx.doi.org/10.1021/la500355f.

[49] S. Yang, H. Zhang, S.M. Hsu, Correction of random surface roughness on colloidal probes in measuring adhesion, Langmuir 23 (2007) 1195–1202, http://dx.doi.org/10.1021/la0622828.

[50] S. Yang, H. Zhang, M. Nosonovsky, K.-H. Chung, Effects of contact geometry on pull-off force measurements with a colloidal probe, Langmuir 24 (2008) 743–748, http://dx.doi.org/10.1021/la701900f.

[51] L.-O. Heim, J. Blum, M. Preuss, H.-J. Butt, Adhesion and friction forces between spherical micrometer-sized particles, Phys Rev Lett. 83 (1999) 3328–3331, http://dx.doi.org/10.1103/PhysRevLett. 83.3328.

[52] E.R. Beach, G.W. Tormoen, J. Drelich, R. Han, Pull-off force measurements between rough surfaces by atomic force microscopy, J. Colloid Interface Sci. 247 (2002) 84–99, http://dx.doi.org/10.1006/jcis.2001.8126.

[53] O. Laitinen, K. Bauer, J. Niinimäki, U.A. Peuker, Validity of the Rumpf and Rabinovich adhesion force models for alumina substrates with nanoscale roughness, Powder Technol. 246 (2013) 545–552, http://dx.doi.org/10.1016/j.powtec.2013.05.051.

[54] P. Prokopovich, V. Starov, Adhesion models: from single to multiple asperity contacts, Adv. Colloid Interface Sci. 168 (2011) 210–222.

[55] S. You, M.P. Wan, Modeling and experiments of the adhesion force distribution between particles and a surface, Langmuir 30 (2014) 6808–6818, http://dx.doi.org/10.1021/la500360f.

[56] R.P. Jaiswal, G. Kumar, C.M. Kilroy, S.P. Beaudoin, Modeling and validation of the van der Waals force during the adhesion of nanoscale objects to rough surfaces: a detailed description, Langmuir 25 (2009) 10612–10623, http://dx.doi.org/10.1021/la804275m.

[57] K. Cooper, A. Gupta, S. Beaudoin, Simulation of particle adhesion: implications in chemical mechanical polishing and post chemical mechanical polishing cleaning, J. Electrochem. Soc. 148 (2001) G662–G667, http://dx.doi.org/10.1149/1.1409975.

[58] K. Cooper, A. Gupta, S. Beaudoin, Simulation of the adhesion of particles to surfaces, J. Colloid Interface Sci. 234 (2001) 284–292, http://dx.doi.org/10.1006/jcis.2000.7276.

[59] S. Eichenlaub, A. Gelb, S. Beaudoin, Roughness models for particle adhesion, J. Colloid Interface Sci. 280 (2004) 289–298, http://dx.doi.org/10.1016/j.jcis.2004.08.017.

[60] Y. Chen, L. Jallo, M.A.S. Quintanilla, R. Dave, Characterization of particle and bulk level cohesion reduction of surface modified fine aluminum powders, Colloids Surf. A 361 (2010) 66–80.

[61] I. Cavarretta, C. O'Sullivan, M.R. Coop, Applying 2D shape analysis techniques to granular materials with 3D particle geometries, in: M. Nakagawa, S. Luding (Eds.), Powders and Grains 2009: Proceedings of the 6th international Conference on Micromechanics of Granular Media, Golden, CO, 2009, pp. 833–836, http://dx.doi.org/10.1063/1.3180057.

[62] C.Q. LaMarche, A.W. Miller, P. Liu, C.M. Hrenya, Linking micro-scale predictions of capillary forces to macro-scale fluidization experiments in humid environments, AIChE J. 62 (2016) 3585–3597, http://dx.doi.org/10.1002/aic.15281.

[63] S.F. Foerster, M.Y. Louge, H. Chang, K. Allia, Measurements of the collision properties of small spheres, Phys. Fluids 6 (1994) 1108–1115, http://dx.doi.org/10.1063/1.868282.

[64] J.T. Dickinson, R.F. Hariadi, L. Scudiero, S.C. Langford, A scanning force microscope study of detachment of nanometer-sized particles from glass surfaces, Tribol. Lett. 7 (1999) 113–119.

[65] B. Cappella, G. Dietler, Force-distance curves by atomic force microscopy, Surf. Sci. Rep. 34 (1999) 1–104.

[66] N. Fernandez, J. Cayer-Barrioz, L. Isa, N.D. Spencer, Direct, robust technique for the measurement of friction between microspheres, Langmuir 31 (2015) 8809–8817, http://dx.doi.org/10.1021/acs.langmuir.5b01086.

[67] Y.I. Rabinovich, J.J. Adler, A. Ata, R.K. Singh, B.M. Moudgil, Adhesion between nanoscale rough surfaces I. role of asperity geometry, J. Colloid Interface Sci. 232 (2000) 10–16, http://dx.doi.org/10.1006/jcis.2000.7167.

[68] S. Eichenlaub, G. Kumar, S. Beaudoin, A modeling approach to describe the adhesion of rough, asymmetric particles to surfaces, J. Colloid Interface Sci. 299 (2006) 656–664.

[69] D. Kunii, O. Levenspiel, Fluidization Engineering, 2nd ed., Butterworth-Heinemann, Boston, 1991.

[70] G.G. Joseph, J. Leboreiro, C.M. Hrenya, A.R. Stevens, Experimental segregation profiles in bubbling gas-fluidized beds, AIChE J. 53 (2007) 2804–2813, http://dx.doi.org/10.1002/aic.11282.

[71] J.F. Richardson, Incipient fluidization and particulate systems, in: J.F. Davidson, D. Harrison (Eds.), Fluidization, American Press, New York, 1971, pp. 25–64.

[72] D. Gauthier, S. Zerguerras, G. Flamant, Influence of the particle size distribution of powders on the velocities of minimum and complete fluidization, Chem. Eng. J. 74 (1999) 181–196.

[73] H.Y. Xie, D. Geldart, Fluidization of FCC powders in the bubble-free regime: effect of types of gases and temperature, Powder Technol. 82 (1995) 269–277.

[74] J. Werther, O. Molerus, The local structure of gas fluidized beds—II. The spatial distribution of bubbles, Int. J. Multiphase Flow 1 (1973) 123–138.

[75] D. Geldart, Types of gas fluidization, Powder Technol. 7 (1973) 285–292.

[76] P.C. Carman, Fluid flow through granular beds, Trans. Instit. Chem. Eng. 15 (1937) 150–166.

[77] J.M. Valverde, A. Castellanos, P. Mills, M.A.S. Quintanilla, Effect of particle size and interparticle force on the fluidization behavior of gas-fluidized beds, Phys. Rev. E 67 (2003) 051305.

[78] D. Geldart, N. Harnby, A.C. Wong, Fluidization of cohesive powders, Powder Technol. 37 (1984) 25–37.

[79] S.C. Tsinontides, R. Jackson, The mechanics of gas fluidized beds with an interval of stable fluidization, J Fluid Mech. 255 (1993) 237–274.

[80] A.R. Abrahamsen, D. Geldart, Behaviour of gas-fluidized beds of fine powders part I. Homogeneous expansion, Powder Technol. 26 (1980) 35–46, http://dx.doi.org/10.1016/0032-5910(80)85005-4.

[81] E. Jaraiz, S. Kimura, O. Levenspiel, Vibrating beds of fine particles: estimation of interparticle forces from expansion and pressure drop experiments, Powder Technol. 72 (1992) 23–30.

[82] J.K. Pandit, X.S. Wang, M.J. Rhodes, On Geldart group A behaviour in fluidized beds with and without cohesive interparticle forces: a DEM study, Powder Technol. 164 (2006) 130–138, http://dx.doi.org/10.1016/j.powtec.2006.03.007.

[83] M. Ye, M.A. van der Hoef, J.A.M. Kuipers, The effects of particle and gas properties on the fluidization of Geldart A particles, Chem. Eng. Sci. 60 (2005) 4567–4580, http://dx.doi.org/10.1016/j.ces.2005.03.017.

[84] M. Ye, M.A. van der Hoef, J.A.M. Kuipers, A numerical study of fluidization behavior of Geldart A particles using a discrete particle model, Powder Technol. 139 (2004) 129–139, http://dx.doi.org/10.1016/j.powtec.2003.10.012.

[85] M. Horio, A. Nonaka, A generalized bubble diameter correlation for gas-solid fluidized beds, AIChE J. 33 (1987) 1865–1872.

[86] H.R. Norouzi, N. Mostoufi, Z. Mansourpour, R. Sotudeh-Gharebagh, J. Chaouki, Characterization of solids mixing patterns in bubbling fluidized beds, Chem. Eng. Res. Des. 89 (2011) 817–826.

[87] A.B. Yu, C.L. Feng, R.P. Zou, R.Y. Yang, On the relationship between porosity and interparticle forces, Powder Technol. 130 (2003) 70–76.